THE JOURNAL OF PHYSICAL CHEMISTRY LETTERS
A JOURNAL OF THE AMERICAN CHEMICAL SOCIETY

pubs.acs.org/JPCL

Perspective

Surface Plasmons in Two-Dimensional MXenes

Calvin Raab, Janek Rieger, Atreyie Ghosh, Joseph L. Spellberg, and Sarah B. King*

Cite This: *J. Phys. Chem. Lett.* 2024, 15, 11643−11656

Read Online

ACCESS | Metrics & More | Article Recommendations

ABSTRACT: MXenes, a class of layered two-dimensional transition metal carbides and nitrides, exhibit excellent optoelectronic properties and show promise for fields ranging from photonics and communications to energy storage and catalysis. Some members of the MXene family are metallic and exhibit large in-plane conductivity, making them possibly suited for 2D plasmonics. The highly variable chemical structure of MXenes offers a broad chemical space to tune material properties for plasmonic applications, including plasmon-enhanced catalysis, surface-enhanced Raman spectroscopy (SERS), and electromagnetic shielding. However, this synthetic complexity has also presented several roadblocks in the process of moving MXene plasmonics into applications. For example, in the prototypical MXene $Ti_3C_2T_x$, there remains disagreement over the bulk plasmon energy and the assignment of a prominent resonance around 1.7 eV. We discuss fundamental models and theories of plasmon physics and apply these models to MXenes in order to clarify some of these problems. We outline the potential for hyperbolic plasmons in MXenes and propose new avenues for MXene photonics research.

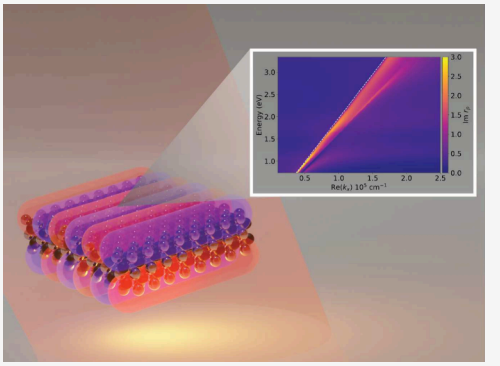

1. INTRODUCTION

The rise of two-dimensional layered materials has been one of the most significant developments in twenty-first century condensed matter physics and materials science. Beginning with the discovery of graphene, 2D materials have exploded into a diverse field with the potential to showcase a variety of novel physical phenomena.[1,2] The tunability and unique optoelectronic properties of 2D materials present an excellent platform for enhancing light−matter interactions for photonics.[3−6] For instance, plasmonic modes in 2D materials offer extreme spatial confinement of light in thin films, resulting in the potential to control light at the nanoscale.[3,4,7] Nanophotonics applications such as optical circuitry, plasmonic sensors, and plasmonic catalysis can utilize this confinement to great advantage.[8] In addition, the optoelectronic properties of 2D materials can be tuned by thickness as well as by doping, gating, and integration into heterostructures.[9,10] Plasmonic phenomena in 2D materials were first documented in semimetal graphene in the THz to mid-IR region of the spectrum.[11] This discovery generated a large amount of interest due to graphene's low losses compared to noble metals and the ability to tune the plasmonic energy by doping and gating.[6,10,11] The emergence of graphene plasmonics has sparked a search for other 2D materials that might be suitable for similar plasmonic applications.[3,5]

Recently, MXenes, a group of transition metal carbides and nitrides, have arisen as another potential platform for 2D plasmonics.[12,13] MXenes have the general formula $M_{n+1}X_nT_x$, where M is an early transition metal (such as titanium, vanadium, or molybdenum), X is carbon or nitrogen, and T is a variable surface termination such as −O, −OH, −Cl, and −F. The atomic structures of two prototypical MXenes, $Ti_3C_2T_x$ and Ti_2CCl_2, are shown in Figure 1. A single layer of MXene consists of a hexagonal lattice of the transition metal and the carbide/nitride, the surface of which can be functionalized with a variety of main group terminations. Interlayer interactions may be dipole−dipole, hydrogen bonding, or van der Waals interactions depending on the surface termination type.[14]

The plethora of available MXene structures enables synthetic tailoring of MXenes for particular properties such as conductivity or optical absorbance.[15] For example, most MXenes are metals, but some species (such as Ti_2CO_2) are predicted to be semiconductors.[16,17] One of the central appeals of MXenes is that they combine properties common to metals (such as high conductivity) with properties useful for wet chemistry (such as tunable surface groups and hydrophilicity).[18] This unique combination enables a variety of applications. For instance, MXene powders can be easily dispersed in aqueous solvents that can be used to create inks for printing patterned devices or sprayed into conductive thin-film coatings.[19] With both strong optical absorption signatures

Received: October 3, 2024
Revised: November 5, 2024
Accepted: November 7, 2024
Published: November 14, 2024

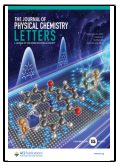

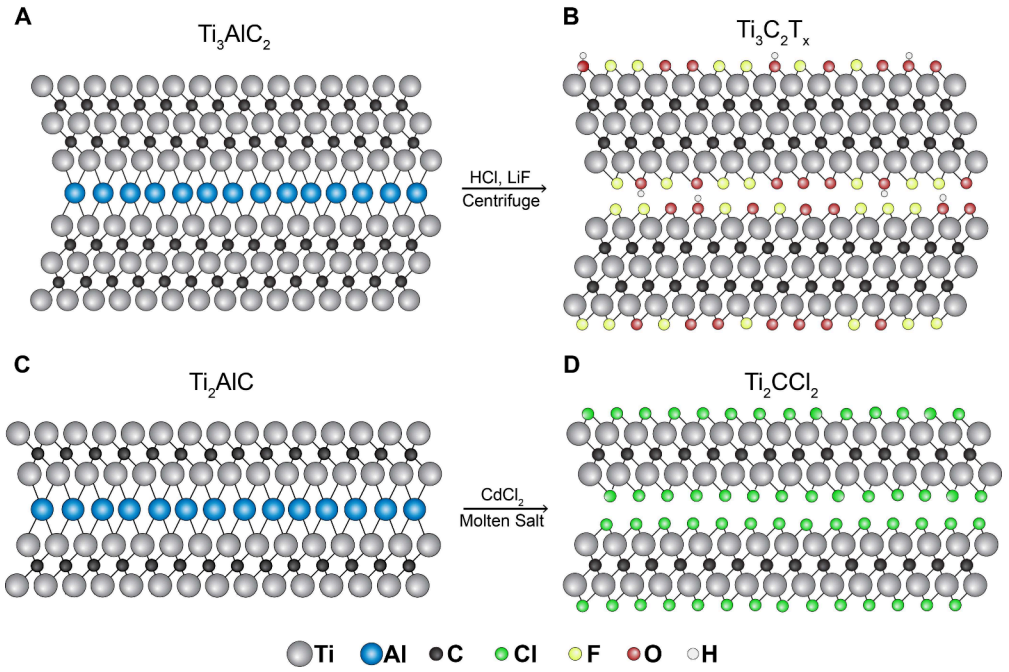

Figure 1. Structure and synthesis of exemplary MXenes $Ti_3C_2T_x$ (top) and Ti_2CCl_2 (bottom). (A) The precursor MAX phase of Ti_3AlC_2 used in the synthesis of the mixed termination MXene with *in situ* HF (B) $Ti_3C_2T_x$. (C) The precursor MAX phase Ti_2AlC is used with a molten salt synthesis to form the single terminated (D) Ti_2CCl_2 material.

and metallic reflectivity, MXenes are candidates for broadband electromagnetic shielding.[20,21] MXenes can also easily intercalate ions within their interlayer spaces, which means they could serve as supercapacitors for energy storage or as electrodes for electrochemical reactions.[19] More unusual properties can also be achieved in MXenes such as Nb_2CS_2 and Nb_2CSe_2, which show superconductivity.[22] The stacking of few-layer Ti_3C_2 MXenes has been demonstrated to create moiré patterns reminiscent of those observed in twisted bilayer graphene, possibly suggesting that MXenes could be used for twistronics.[23] Along with the properties mentioned above, metallic MXenes are excellent candidates for plasmonics. In this Perspective, we focus on the plasmonic properties of MXenes, with a particular emphasis on the plasmonic behavior of the mixed terminated MXene $Ti_3C_2T_x$.

$Ti_3C_2T_x$, where T is −O, −OH, and −F, is the most well studied and synthetically facile MXene and will therefore be the central focus of this report. However, the fundamental principles of plasmon physics that will be discussed for 2D layered metals will be generally valid for all other classes of MXenes. The mixed terminated MXene is created by etching of MAX phase Ti_3AlC_2 (Figure 1A) with hydrofluoric acid (HF) generated *in situ*, which removes the aluminum layer and leaves the random mixture of −O, −OH, and −F terminations on the surface (Figure 1B). In addition to such mixed terminated materials, MXenes with single halide terminations such as Ti_2CCl_2 (Figure 1D) are promising systems for plasmonics and can be synthesized by Lewis acid molten salt etching techniques and chemical vapor deposition (CVD).[22,24,25]

Due to their metallic nature, $Ti_3C_2T_x$ MXenes can support plasmonic resonances in the near-infrared (NIR) region. This was first demonstrated by Mauchamp et al.,[26] who showed the existence of NIR surface plasmons in MXene flakes using electron energy loss spectroscopy (EELS). EELS imaging by El-Demellawi et al.[27] identified tunable, localized surface plasmons in isolated MXene flakes. Additional work has also shown the dispersion relationships of MXene surface plasmons and their thickness dependence in this energy range.[28,29] Measurements from our previous research using photoemission electron microscopy (PEEM) have also revealed the presence of long propagation length plasmons (so-called long-range surface plasmons or LRSPs) up to 1.9 eV.[30,31] With the groundwork laid, proposed photonic devices utilizing MXene plasmonics have begun to appear. These include using MXenes for surface-enhanced Raman spectroscopy (SERS), wearable photothermal devices, THz shielding, and metamaterials for optical photodetection.[12,32−34] Here again, the distinct advantage of MXenes is their chemically active surface. Plasmon-enhanced catalysis, for instance, relies on excited carriers generated by plasmonic dissipation, which could enhance the activity of the already catalytically active MXene surface.[35] Despite these advances, there still remain many unknowns in our understanding of MXene plasmonics. The inherent structural complexity of this material, while undoubtedly useful for applications, makes understanding the optoelectronic properties of MXenes much more challenging than for many other 2D materials, such as graphene and transition metal dichalcogenides (TMDCs). Several important material properties remain controversial in the literature, including bulk plasmon energies, the assignment of prominent optical resonances, and the material dielectric function. As MXenes continue to find new applications, the importance of addressing these fundamental questions will increase.

In this Perspective, we discuss previous work on MXene plasmonics and apply the fundamentals of plasmon physics to clarify some of the disagreements in the literature. While MXenes are 2D layered materials, there are different ways to consider their 2D nature, depending on the approximations that are used. To be comprehensive, we start with the simplest model of a bulk, isotropic three-dimensional Drude metal and then consider semi-infinite interfaces and finally more complex

https://doi.org/10.1021/acs.jpclett.4c02882
J. Phys. Chem. Lett. 2024, 15, 11643−11656

thin-film models that can take into account anisotropic dielectric functions. We compare published literature results on MXenes' charge carrier density, bulk plasmon energy, and interband transition (IBT) assignments with these models. We also comment on the potential for MXenes to support hyperbolic plasmons due to strong out-of-plane anisotropy and discuss potentially fruitful new avenues for MXene plasmonics research.

2. BULK PLASMONS AND CHARGE CARRIER DENSITY

Understanding the plasmonic behavior of materials begins with considering the volume or bulk plasmon. This longitudinal charge oscillation occurs in the bulk without regard to interfaces and requires that the real part of the frequency-dependent dielectric function $\varepsilon(\omega) = \varepsilon'(\omega) + i\varepsilon''(\omega)$ is equal to zero.[42,43] This bulk plasmon energy is the natural resonance energy of the charge carriers and may be observed as a large peak in the electron energy loss function $\mathrm{Im}(-1/\varepsilon)$, shown as ω_p in Figure 2.[44] For the simplest case where the metal approximates an isotropic free electron gas, the electronic response can be described by the Drude model,

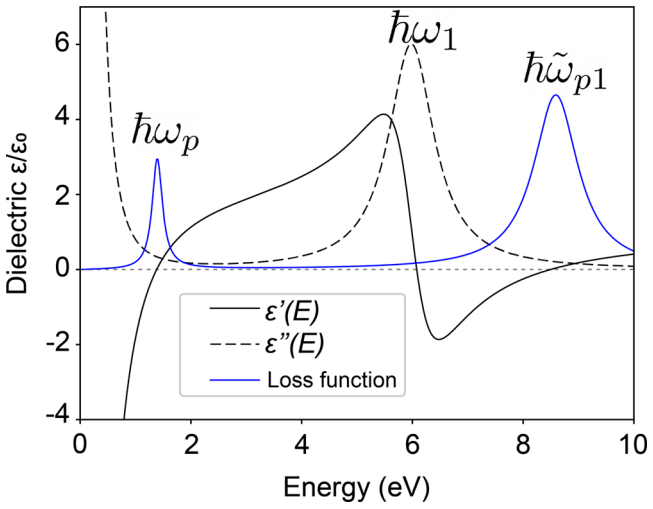

Figure 2. Calculation of contributions from free and bound electrons to the dielectric function based on free electron and bound electron responses of a model metal. The Drude (free electron) response causes a peak in the electron energy loss function which corresponds to the bulk plasmon at $\hbar\omega_p$. The Lorentzian bound electron response in the real and imaginary components of the dielectric function at $\hbar\omega_1$ leads to a peak in the imaginary component of the dielectric function at $\hbar\omega_1$. As the real portion of the dielectric briefly becomes negative at energies higher than $\hbar\omega_1$ before recrossing zero at $\hbar\tilde{\omega}_{p1}$, this leads to a second, higher energy bulk plasmon and loss function peak at $\hbar\tilde{\omega}_{p1}$.

$$\varepsilon(\omega)/\varepsilon_0 = 1 - \frac{\omega_p^2}{\omega^2 + i\omega\Gamma} \quad (1)$$

where ω_p is the Drude frequency and Γ is a phenomenological damping factor accounting for losses from mechanisms such as electron−phonon and electron−electron scattering and electron−hole excitation.[43,45] This places the free electron bulk plasmon energy at the Drude frequency $\omega_p = \sqrt{\frac{ne^2}{m_e^* \epsilon_0}}$, with a square root dependence on the free charge density n and the effective mass m_e^*.[11,46] Unless otherwise specified, m_e^* is here assumed to be m_e since this is generally assumed for electrical conductivity experiments. The precise determination of m_e^* requires either rigorous band structure calculations or experiments such as magnetic circular dichroism spectroscopy.[47,48] In an ideal metal without interband transitions (IBTs), the Drude energy determines the optical properties of the material. Below this energy, the dielectric is negative, and incident light is reflected from the material due to efficient screening; above this energy, the dielectric function is positive, and the material can transmit light. For example, the Drude energy for aluminum, a metal well approximated by the free electron model, is 12.5 eV.[47] In MXenes, the Drude energy, along with the related charge carrier density, has been a subject of disagreement within the literature (see Table 1 for a comparison of literature results). Dillon et al.[41] found a charge carrier density of 3×10^{22} $e{\cdot}\mathrm{cm}^{-3}$ ($\hbar\omega_p$ = 6.54 eV) with Hall effect measurements, while Miranda et al.[37] found a value around 8.0×10^{21} $e{\cdot}\mathrm{cm}^{-3}$ ($\hbar\omega_p$ = 3.32 eV). On the other hand, the EELS measurements from El-Demellawi et al.[27] identified a substantively lower density at 1.6×10^{21} $e{\cdot}\mathrm{cm}^{-3}$ ($\hbar\omega_p$ = 1.49 eV). A similar value was reported by Li et al.[36] at 1.66×10^{21} $e{\cdot}\mathrm{cm}^{-3}$ using THz spectroscopy and an effective mass $m_e^* = 0.2845 m_0$.[49] Values derived from spectroscopic ellipsometry data have yielded Drude energies ranging from 3 to 6 eV, which correspond to charge densities from 1×10^{22} to 2.5×10^{22} $e{\cdot}\mathrm{cm}^{-3}$,[29,39,40] as shown in Table 1.

Table 1. Literature Experimental Values for Drude Energy and Charge Density

Charge Density ($e{\cdot}\mathrm{cm}^{-3}$)	Drude Energy (eV)	Method	Ref
1.60×10^{21}	1.49	EELS	El-Demellawi et al.[27]
2.0×10^{21}	1.66	THz Spectroscopy	Li et al.[36]
7.61×10^{21}	3.24	EELS	Guo et al.[29]
8.0×10^{21}	3.32	Electrical $I-V$ Curve	Miranda et al.[37]
8.66×10^{21}	3.45	Spectroscopic Ellipsometry	Lioi et al.[38]
1.10×10^{22}	3.9	Spectroscopic Ellipsometry	Chaudhuri et al.[39]
2.53×10^{22}	5.91	Spectroscopic Ellipsometry	Shamsabadi et al.[40]
3.10×10^{22}	6.54	Hall Effect	Dillon et al.[41]

The variations in the observed carrier densities and bulk plasmon energy may originate from several sources. In $Ti_3C_2T_x$, difficulty in controlling terminations and variations in synthetic procedures introduce variability in sample properties. For example, even different flake delamination procedures involving postsynthetic centrifugation or sonication can impact the size and quality of flakes.[50−52] Additional factors such as contamination from oxidation or water intercalation could also play a role in affecting electronic properties.[53,54] Another issue is that large-scale electrical measurements of MXene films may not be able to distinguish between intra- and interflake conduction.[38,41,55] Additionally, some sources do not make clear the value of m_e^* used when calculating n from the measured DC conductivity $\sigma(0)$. When $m_e^* = m_e$ is used, any corrections to the free electron model are incorporated into an effective charge density $n = n_{\mathrm{eff}}$, whereas using m_e^* from band structure calculations gives values of n that directly correspond to the number of valence electrons per unit cell.[47]

https://doi.org/10.1021/acs.jpclett.4c02882
J. Phys. Chem. Lett. 2024, 15, 11643−11656

The Drude energies and charge density mentioned above are, despite their variation, all located <7 eV. In contrast to these values, a large peak appears in the electron loss spectrum at 23−24 eV and has been attributed to a bulk plasmon.[26,28] However, for a Drude model, this would yield a free charge density of over 4×10^{23} $e{\cdot}cm^{-3}$, which is significantly higher than even that of aluminum at 1.1×10^{23} $e{\cdot}cm^{-3}$.[47] The origin of the 23−24 eV peak is most likely due to contributions from bound electrons, and accounting for this requires a more sophisticated model than the free electron model.[42,44]

While the free electron response can be understood with a Drude model, bound electrons (such as valence electrons in semiconductors) have a natural resonance frequency ω_i that corresponds to an optical interband transition (IBT). Therefore, the total charge density is the sum of free (f) and bound (b) electrons, $n = n_f + n_b$, and the dielectric function is given by $\varepsilon(\omega) = \varepsilon_f(\omega) + \varepsilon_b(\omega)$. The free electron contribution $\varepsilon_f(\omega)$ is simply the Drude dielectric function (eq 1), while the bound contribution is given by a sum of Lorentzians for each electronic transition,

$$\varepsilon_b(\omega)/\varepsilon_0 = \sum_i \frac{\omega_{pi}^2}{\omega_i^2 - \omega(\omega + i\Gamma_i)} \tag{2}$$

where $\omega_{pi} = \sqrt{\frac{n_{bi}e^2}{m_e\varepsilon_0}}$ describes the oscillator strength and Γ_i and n_{bi} are the damping and bound charge densities for each interband transition, respectively.[42] Assuming the IBTs are far enough apart not to interact and losses are small, a bulk plasmon peak ($\varepsilon'(\omega) = 0$ and $\frac{\partial\varepsilon'(\omega)}{\partial\omega} > 0$) due to bound electrons occurs at $\tilde{\omega}_{pi} = \sqrt{\omega_i^2 + \omega_{pi}^2}$ for each IBT term i (as illustrated by $\tilde{\omega}_{pi}$ in Figure 2).[42] It is important to note that the bound bulk plasmon due to the zero of $\varepsilon(\omega)$ at $\tilde{\omega}_{pi}$ should not be confused with the zero of $\varepsilon(\omega)$ at ω_i. Due to the sign of the slope ($\frac{d\varepsilon'(\omega)}{d\omega}\Big|_{\omega=\omega_i} < 0$), ω_i corresponds to an optically active IBT peak in $\varepsilon''(\omega)$ rather than a bulk plasmon.[43,44] This is demonstrated in Figure 2, where the bulk plasmon $\hbar\tilde{\omega}_{p1}$ corresponds to a loss function peak whereas the optical IBT is associated with a peak in $\varepsilon''(\omega)$ at $\hbar\omega_1$. Caution is needed here since loss function peaks at $\hbar\tilde{\omega}_{pi}$ may be referred to as IBT peaks in the literature because they always occur just above the IBT energy.[56] In complicated spectra with multiple resonances, IBTs might not cause zeros in the dielectric function at either $\hbar\omega_i$ or $\hbar\tilde{\omega}_{pi}$, though they still have associated loss function peaks that are not plasmonic in nature.

Because of additive contributions to the dielectric function from intraband Drude and interband Lorentzian terms, the zeros of $\varepsilon'(\omega)$ may be shifted from $\hbar\omega_p$ or $\hbar\tilde{\omega}_{pi}$. Thus, the presence of IBTs can both shift the energy of free electron bulk plasmons and induce additional bulk plasmon resonances from the bound electrons. In Figure 2, this is demonstrated for an ideal system where bulk plasmons exist at both $\hbar\omega_p$ and $\hbar\tilde{\omega}_{p1}$ due to free and bound electrons, respectively. An example of this phenomenon can be found in semiconductors where there exist both low-energy plasmons from conduction band electrons in the THz to IR range and higher energy plasmons in the 15−25 eV range from valence band electrons.[44] For example, in graphite the bulk plasmon peaks at 7 and 28 eV occur due to π and π+σ electrons, respectively.[57] The peak in the MXene loss spectrum at 24 eV appears to be such a bulk plasmon of *bound* electrons rather than the bulk plasmon of free electrons.[58] The intensity of the peak suggests a bulk plasmon rather than a nonplasmonic peak induced by an IBT and can be distinguished from surface effects by the dependence of the EELS peak intensity on thickness.[26,44]

While the most suitable method for identifying bulk plasmons is from the loss spectrum, definitive assignment of interband transitions requires both the optical dielectric function and high-quality electronic band structures. Determination of band structures requires both theory calculations and spectroscopic techniques, such as angle-resolved photoemission spectroscopy (ARPES). The dielectric function, on the other hand, can be determined experimentally from either spectroscopic ellipsometry or EELS. Ellipsometric data provides the complex reflectance ratio r_p/r_s for s- and p-polarized light which can be converted to a dielectric function by fitting to a known model (typically a Drude−Lorentz model).[39,40] EELS can yield the loss function $\mathrm{Im}(-1/\varepsilon)$, from which both ε' and ε'' may be determined along with surface and multipole contributions.[44,59]

Various dielectric functions of MXenes have been obtained from both theory and experiment. Lashgari et al.[60] used DFT methods to determine both the band structure and the optical permittivity of Ti_3C_2 and Ti_2C MXenes. This work predicted several IBTs in the relevant energy range, the most prominent of which was centered at 1.8 eV, with additional resonances at 3.2, 4.2, and 5.4 eV. Spectroscopic ellipsometry experiments on MXenes have also been used to determine dielectric functions in the IR-visible range as shown in Figure 3A. These experiments show a prominent Lorentzian around 1.5−1.7 eV with another Lorentzian typically located in the 3.5−4 eV or 4.8−5.4 eV range.[38−40] The impact of these Lorentzian terms can be seen in Figure 3A, where the first zero of $\varepsilon'(\omega)$ is pushed well below the estimations for ω_p from Table 1 into the NIR.

Dielectric functions from Chaudhuri et al.[39] and Shamsabadi et al.[40] in Figure 3A also show a region of $\varepsilon'(\omega) < 0$ that begins at ∼1.5 eV due to a Lorentzian feature in this region. While there is consensus that there are both strong optical absorbance and EELS peaks in $Ti_3C_2T_x$ MXenes around 1.7 eV, the nature of this resonance remains contested. It is important to note that the optical absorbance due to a peak in $\varepsilon''(\omega)$ is different than the loss function peak at slightly higher energy (see model spectrum in Figure 2). While there is an IBT influence evident due to the Lorentzians in Figure 3A at ∼1.5 eV, there are also associated loss peaks in Figure 3B at slightly higher energy. The variability in the reported dielectric functions makes it difficult to assign the nature of this loss peak. For example, the dielectric in Shamsabadi et al.[40] shows a zero in $\varepsilon'(\omega)$ for this loss peak, implying a bulk plasmon; however, the other reported dielectric functions do not show a zero at this energy. El-Demellawi et al.[27] assigned this mode to a transversal surface plasmon, noting its independence from flake lateral dimensions. Another piece of evidence is that annealing to remove −F terminations causes an increase in the energy of the mode, which is also correlated with an increase in the calculated charge density. In contrast, the agreed upon IBT at 3.5 eV shows no such dependence. On the other hand, electronic structure calculations of Ti_3C_2 suggest an IBT in the relevant energy range.[60−62] The universality of this peak suggests that it is intrinsic to the dielectric function and not geometrically dependent. Further details of this disagreement

https://doi.org/10.1021/acs.jpclett.4c02882
J. Phys. Chem. Lett. 2024, 15, 11643−11656

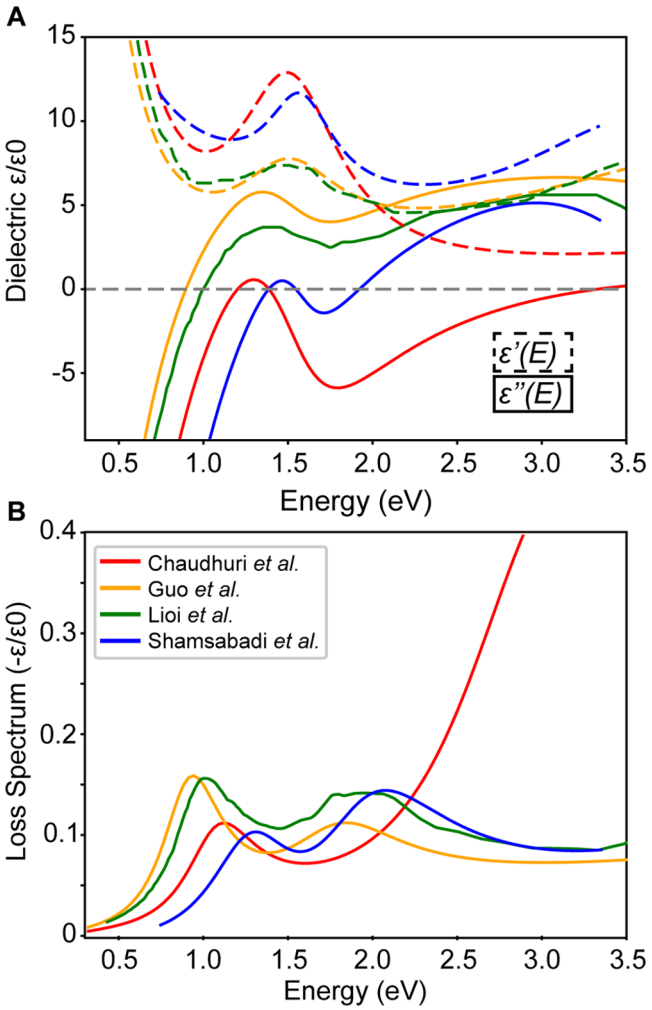

Figure 3. Comparison of experimental $Ti_3C_2T_x$ MXene dielectric functions (A) and corresponding calculated loss spectra (B). (A) Solid lines show the real part of the dielectric function $\varepsilon'(\hbar\omega)$; dotted lines show the imaginary part $\varepsilon''(\hbar\omega)$. The dielectrics from Chaudhuri, Lioi, and Shamsabadi et al. were determined by spectroscopic ellipsometry, whereas that from Guo et al. is from fitting EELS data.[29,38−40] Note the impact of Lorentzian peaks on the location of the zeros of $\varepsilon'(\hbar\omega)$. (B) The loss function $\mathrm{Im}(-1/\varepsilon)$ gives a spectrum proportional to that seen in EELS experiments and shows peaks at bulk plasmon energies.

will be discussed in the section dealing with localized plasmons.

3. SURFACE PLASMON MODES

While bulk plasmons occur due to volume charge oscillations, the presence of an interface with a dielectric medium allows for oscillations of charges confined to the metal surface. This results in a surface plasmon, depicted schematically in Figure 4A. In contrast to the dispersionless bulk plasmon, a surface plasmon polariton (SPP) propagating in the $+x$ direction has a dispersion $\omega(k_x)$ that depends on the plasmonic wavevector $\vec{k}_i = k_x\hat{x} + k_{iz}(\omega,k_x)\hat{z}$ and the permittivities, ε_1 and ε_2, of the dielectric and metal, respectively. The dispersion (idealized in Figure 4B and shown for a Drude metal in Figure 4C) for this semi-infinite mode can be found by determining the poles of the reflection coefficient, r_p, for p-polarized light.[56]

$$r_p = \frac{\epsilon_1(\omega)k_{2z}(\omega, k_x) - \epsilon_2(\omega)k_{1z}(\omega, k_x)}{\epsilon_1(\omega)k_{2z}(\omega, k_x) + \epsilon_2(\omega)k_{1z}(\omega, k_x)} \quad (3)$$

$$k_{iz}(\omega, k_x) = \sqrt{\varepsilon_i\frac{\omega^2}{c^2} - k_x^2} \quad (4)$$

The pole of r_p gives the dispersion condition $\epsilon_1 k_{2z} + \epsilon_2 k_{1z} = 0$. To meet this condition, the real portions of the dielectric functions, ε_1' and ε_2', must have opposite signs. For a metal/dielectric medium interface where the dielectric medium has a positive real permittivity, plasmons can therefore only occur where the metal dielectric function $\varepsilon_2' < 0$. This is the most important condition for determining the potential presence of surface plasmons and will generally hold for more complicated geometries.[63] Additionally, most media only allow transverse magnetic (TM) polarized solutions because of magnetic field boundary conditions and transverse electric (TE) modes are forbidden.[63] In Figure 4D, it is apparent that this results in a pinwheel-like electric field emanating from the charges on the interface.

The dispersive behavior of the semi-infinite surface plasmon can be seen by writing the explicit frequency-dependent dispersion of $k_x(\omega)$,[56]

$$k_x = \frac{\omega}{c}\sqrt{\frac{\varepsilon_1(\omega)\varepsilon_2(\omega)}{\varepsilon_1(\omega) + \varepsilon_2(\omega)}} \quad (5)$$

There are two equivalent conventions to express the dispersion: either using complex $k_x = k_x' + ik_x''$ and real frequency ω or vice versa.[65] We assume $k_x = k_x' + ik_x''$ unless otherwise noted. A simple way to visualize the dispersion using real k_x is to plot a heatmap of $\mathrm{Im}(r_p(k_x',E))$, as done in Figure 4C for a Drude metal. The green solution overlaid on the heatmap shows the alternate formalism using $\omega(k_x' + ik_x'')$. At low energy, the plasmon follows the linear light-line $\omega = ck_x'$ (Figure 4B,C) but reaches an asymptote at the surface plasmon energy ω_{sp}, where $\varepsilon_1(\omega) = -\varepsilon_2(\omega)$. For a Drude metal, $\omega_{sp} = \omega_p/(\sqrt{1+\varepsilon_1})$.[46] In the asymptotic region, k_x' becomes much larger than the light-line momentum $k_0 = \omega/c$, which also results in an increase in vertical spatial confinement k_z'' (eq 4). This is also accompanied by a decrease in propagation length $1/k_x''$ due to losses. The increase in k_x' beyond $k_0 = \omega/c$ is characteristic of SPPs.[11,46] Because of the increased momentum of the SPP, this region is optically inaccessible without a coupling mechanism to supply the required momentum.[56]

The extent of the asymptotic behavior of the semi-infinite dispersion at the resonance frequency ω_{sp} depends on the lossiness of the medium. Because k_x is complex-valued, the dispersion will always reach a maximum k_x^{max} before bending back toward the light line. This behavior is seen clearly in the green solution $\omega(k_x' + ik_x'')$. in Figure 4C. While the heatmap plot of $\mathrm{Im}(r_p)$ instead shows a divergence in k_x since k_x is assumed real, the back-bending at ω_{sp} is seen in the result with complex k_x. The more lossy a material is, the smaller k_x^{max} will be and the weaker the resonance.[11] The lack of a well-defined asymptote significantly reduces the spatial confinement and plasmonic behavior. In addition to a surface plasmon resonance, the presence of a Lorentzian peak due to an IBT can cause a kink in the dispersion at $\omega = \omega_i$ similar to the asymptote at ω_{sp}. If this corresponding peak in $\varepsilon''(\omega)$ has a sufficiently large maximum, then it can even force the dispersion to the left of the light line. Thus, the presence of

https://doi.org/10.1021/acs.jpclett.4c02882
J. Phys. Chem. Lett. 2024, 15, 11643−11656

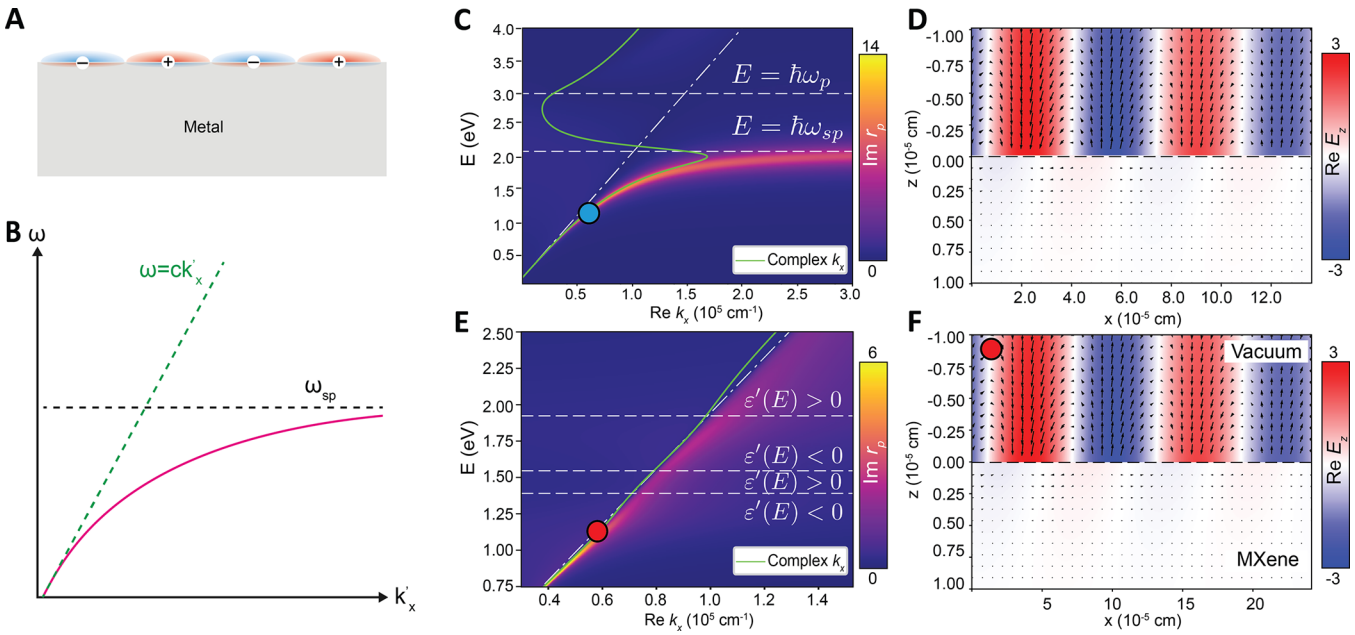

Figure 4. Semi-infinite surface plasmons fields and dispersions for an ideal Drude metal and $Ti_3C_2T_x$ MXene in a vacuum. (A) Illustration of an idealized surface plasmon consisting of oscillating surface charges at a metal/dielectric interface. (B) Schematic of the surface plasmon dispersion which initially follows the light line $E = \hbar ck_x'$ before reaching an asymptote at the surface plasmon resonance. (C) The dispersion of the Drude metal surface plasmon using the colorplot of $\mathrm{Im}(r_p)$ to find $\omega(k_x') = \omega' + i\omega''$. The overlaid solution in green shows the equivalent formalism $\omega(k_x' + ik_x'')$ using a fully complex k_x and real ω. Both the asymptote and lossy "bendback" of $k_x'(\omega)$ at $\hbar\omega_{sp}$ = 2.1 eV may be observed. (D) Real-space electric field distributions for a Drude metal/vacuum interface at 1.15 eV (indicated by a blue dot on the dispersion) showing characteristic plasmonic "pinwheel" fields. (E) The dispersion for the MXene/vacuum surface plasmon polariton with a heatmap of $\mathrm{Im}(r_p)$ and the exact solution in green superimposed. Large losses push the solution to the left of the dashed light line $\omega = ck$ and inhibit formation of a surface plasmon resonance. (F) Real-space electric field distributions for a MXene/vacuum interface (calculated from the dielectric in Shamsabadi et al.[40]) at $\hbar\omega_{sp}$ = 1.15 eV (red dot on dispersion).

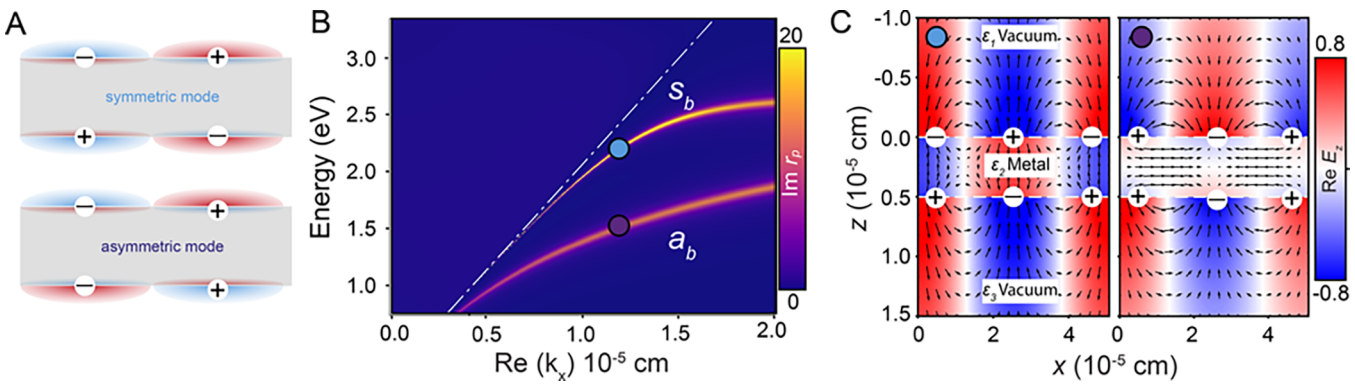

Figure 5. (A) Thin-film surface plasmons show two coupled modes characterized by the symmetry of the charges at either interface, the symmetric upper mode and the asymmetric lower mode.[64] (B) The dispersion of these two film modes for an idealized vacuum/50 nm Drude metal/vacuum interface with the two distinct lower (a_b) and upper (s_b) modes. (C) Electric field distributions for the thin-film modes, with a symmetric E_z for s_b in the blue dot and an asymmetric E_z for a_b in the purple dot.

strong interband transitions, with their associated losses, can significantly impact both the intensity and energy of surface plasmonic resonances.

The influence of such losses on the plasmonic behavior of MXenes appears to be quite large. A survey of the dielectric functions in Figure 3A shows the Lorentzian peaks around 1.5−1.7 eV increase ε'' well above ε' as well as pushing the region where $\varepsilon'(\omega) < 0$ lower in energy. Since plasmons are allowed where $\varepsilon' < 0$, this pushes most of the plasmonic region lower in energy and into the NIR, even though the theoretical surface plasmon resonance (ω_{sp}) from the purely Drude model is in the UV at 4.19 eV.[40] The other major effect of the Lorentzian peak is increasing the plasmonic losses, k_x'', which inhibits the formation of a plasmonic resonance. In Figure 4E, it can be observed that the light green curve showing the analytical dispersion of the surface plasmon based on the Shamsabadi et al. dielectric function is confined close to the light line, even around ω_{sp} at 1.15 eV. An analysis of the electric field at ω_{sp} in Figure 4F shows a plasmonic field very similar to that of the metal in Figure 4D. The field in Figure 4F has clear plasmonic character but shows weak spatial confinement and little penetration into the MXene. The semi-infinite dispersion crosses the light line around 1.3 eV and

https://doi.org/10.1021/acs.jpclett.4c02882
J. Phys. Chem. Lett. 2024, 15, 11643−11656

remains to the left of the light line up to the limit of the analyzed energy region.

4. THIN-FILM MODES AND NANOPARTICLES

Two-dimensional materials are typically studied experimentally as thin films placed on a substrate rather than as the semi-infinite materials discussed in the previous section. In thin films, the interaction between the surface plasmon modes at both the upper and lower interfaces must be considered (see Figure 5A).[64] The result of this coupling is two upper and lower supermodes, each classified by their respective transverse electric field symmetries as antisymmetric (a_b) or symmetric (s_b), as shown schematically in Figure 5. The higher energy s_b mode is also known as the long-range surface plasmon (LRSP) and the a_b mode as the short-range surface plasmon (SRSP) since the LRSP shows a much longer propagation length ($1/k_x''$) than the SRSP.[46,56]

To solve for these modes, we can first consider a three-layer thin-film model, where the plasmonic material (ε_2) with thickness d is surrounded by dielectric media ε_1 and ε_3 (Figure 5C). The total reflection coefficient r_p defines the response of a three-layer system to an externally applied field with k-vector $\vec{k}_i = k_x\hat{x} + k_{iz}(\omega,k_x)\hat{z}$ and frequency ω.[56] The poles of r_p define the natural resonance modes of the system.

$$r_p = \frac{r_{12} + r_{23}\, e^{ik_{2z}(\omega,k_x)d}}{1 + r_{12}r_{23}\, e^{2ik_{2z}(\omega,k_x)d}} \tag{6}$$

This produces the dispersion[56]

$$(\varepsilon_2 k_{1z} + \varepsilon_1 k_{2z})(\varepsilon_2 k_{3z} + \varepsilon_3 k_{2z}) + \tag{7}$$

$$(\varepsilon_1 k_{2z} - \varepsilon_2 k_{1z})(\varepsilon_2 k_{3z} - \varepsilon_3 k_{2z})\, e^{2ik_{2z}d} = 0 \tag{8}$$

This equation generally must be solved numerically for $\omega(k_x)$. In the case that medium 1 and medium 3 are equivalent ($\varepsilon_1 = \varepsilon_3$), the dispersion simplifies into two branches:

$$\varepsilon_1 k_{2z} + \varepsilon_2 k_{1z} \coth(ik_{2z}d/2) = 0 \tag{9}$$

$$\varepsilon_1 k_{2z} + \varepsilon_2 k_{1z} \tanh(ik_{2z}d/2) = 0 \tag{10}$$

These solutions correspond to the aforementioned higher energy s_b and lower energy a_b field modes.[31,46] An example of a case where $\varepsilon_1 = \varepsilon_3$ is given in Figure 5, with the dispersions in Figure 5B and the corresponding fields in Figure 5C.

The thickness of the metallic layer modulates the supermode coupling strength, with thinner films showing greater energetic splitting between the two modes, pushing the s_b mode up in energy and the a_b mode down in energy.[31,56] If the film becomes thin enough, the s_b mode can be pushed above the plasmonic region ($\varepsilon' < 0$), resulting in a cutoff thickness.[31] The a_b mode persists even for monolayer materials, with the dispersion becoming $\omega \propto \sqrt{k_x}$.[46] The presence of a cutoff thickness for the s_b plasmon can be important in identifying this mode (see for example Rieger et al.[30]). Very thick samples reduce to the aforementioned semi-infinite case as coupling becomes negligible. The lower mode a_b surface plasmon has been well documented in MXenes for the NIR region and has a weak asymptote in the proximity of 1 eV, as shown in Figure 6A.[29] The upper mode s_b has also been observed in MXenes by Rieger et al. in the region of the Shamsabadi et al. dielectric function (Figure 3A), where $\varepsilon' < 0$ below 1.9 eV using photoemission electron microscopy (PEEM).[30] The dispersion

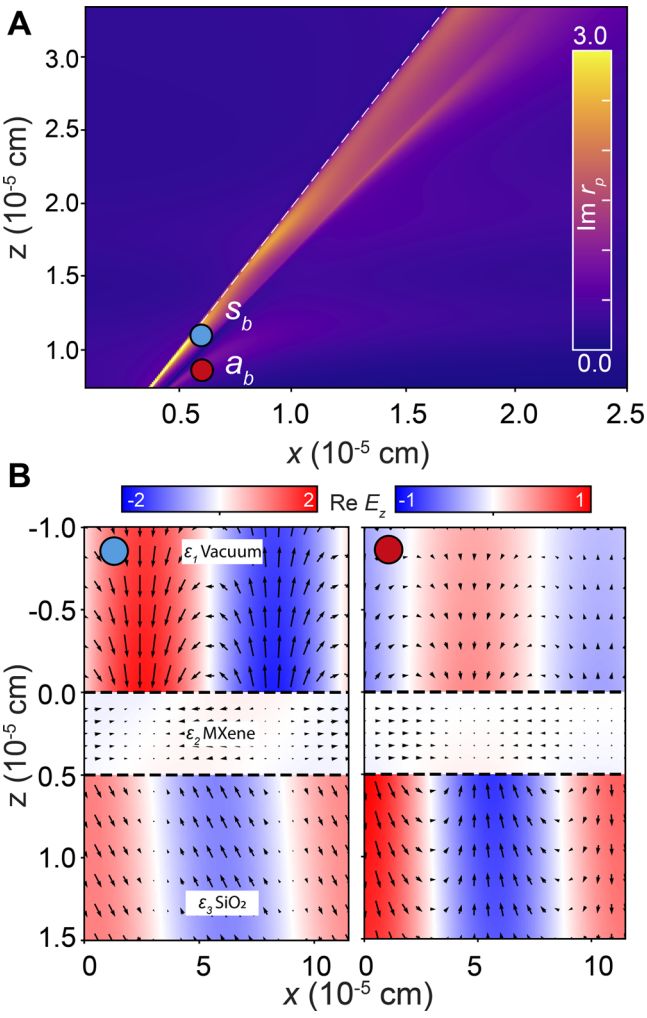

Figure 6. (A) Dispersion of the thin-film vacuum/50 nm MXene/SiO_2 surface plasmons based on the published dielectric function from Shamsabadi et al.[40] (B) Electric field distributions for the s_b and a_b modes of the vacuum/MXene/SiO_2 thin-film geometry.

for this mode is shown in Figure 6A. This experiment shows that the plasmonic region of MXenes extends into the visible portion of the spectrum, despite losses that prevent a plasmonic resonance.

To understand thin-film modes in MXenes, it is necessary to consider not only the MXene layer but also substrate effects since experiments such as PEEM and ellipsometry place MXene flakes on a nonplasmonic substrate. The dispersion for such a case of MXene on silicon dioxide is shown in Figure 6A using the dielectric function of Shamsabadi et al.,[40] showing both the s_b and a_b modes. The s_b mode (blue dot) hugs the light line and transitions into a guided mode above the plasmonic region ($E > 1.9$ eV). The less intense a_b mode (red dot) forms an asymptote around 1 eV in Figure 6A.

It is notable that the thin-film a_b mode has a resonance whereas the semi-infinite mode (Figure 4E) does not. The impact of the substrate is most clear in the electric fields in Figure 6B, as it introduces spatial asymmetry into the electric fields. The s_b mode concentrates the field at the interface with the lower refractive index n, which in this case is the upper interface with the vacuum. On the other hand, the a_b mode concentrates the field at the higher n interface, in this case the lower interface with the SiO_2. The concentration of the s_b field

https://doi.org/10.1021/acs.jpclett.4c02882
J. Phys. Chem. Lett. 2024, 15, 11643−11656

above the MXene results in less confinement within the MXene film. Thus, the s_b mode has a weaker light−matter interaction and less damping. In contrast, the a_b mode will be more strongly confined to the plasmonic medium; however, it will also be more damped. There is, therefore, a trade-off between damping and confinement.[31] Just as in the semi-infinite case, damping plays a major role in the MXene thin-film plasmonic response. The Lorentzian IBT at ∼1.5 eV strongly damps the s_b mode, forcing it to lie close to the light line. Additional damping from the SiO_2 dielectric function also contributes to the backbending of the upper mode.

An additional complication to the thin-film model is that 2D materials typically exist as flakes on the order of hundreds of nanometers to micrometers in diameter; thus, there are also boundary conditions in-plane that depend on the flake geometry. In such nanometer-scale flakes, geometric confinement gives rise to localized surface plasmon resonances (LSPRs). In general, such nanoparticles are dominated by the optically active dipole mode, but shorter wavelengths and nonspherical geometries (e.g., triangles) can result in higher order multipoles modes that are most easily accessible in EELS.[66] In shapes such ellipses or rods with long and short axes, both in- and out-of-plane LSPRs may occur.[67] LSPRs have been documented in MXenes by El-Demellawi et al.[27] as a series of multipolar modes in triangle-like flakes.

While the plasmonic multipolar modes show strong spatial variation, there also exist spatially uniform modes, such as the controversial 1.7 eV mode previously discussed. This mode has been significantly debated in the literature. El-Demellawi et al.[27] assigned this mode to a transversal plasmon due to out-of-plane oscillations, which they analogize to a transversal mode in graphene. However, the transverse electric (TE) surface plasmon is only allowed for a negative imaginary conductivity (unique to graphene) or for magnetically active media, neither of which apply to MXenes.[6,68,69] However, transverse dipole LSPRs may be observed in elliptical or rod-like nanoparticles, due to out-of-plane charge oscillations along the short axis, and other authors claimed this type of LSPR as the origin of this mode.[38,70]

This reported plasmonic transversal mode was addressed by Shamsabadi et al.,[40] who also assigned this mode as a plasmon based on ellipsometry experiments. However, they could not pin down this mode as a either transversal LSPR or a longitudinal LSPR due to a lack of observed optical anisotropy and its lateral size independence.[40,70] Maleski et al.[71] investigated this resonance with reflection and transmission spectroscopy and noted that MXene samples with higher conductivity tended to have the disputed resonance at higher energies, which could be evidence of plasmonic character. However, like Shamsabadi et al.,[40] they found insufficient evidence for what type of plasmonic mode may be present.[71] It is possible that MXene flakes cannot be analogized to an elliptical nanoparticle in terms of producing transverse and longitudinal dipole LSPRs because of the 2D geometry of the flakes.

Lioi et al.[38] examined this resonance using simultaneous ultrafast transmission and reflection (SUTR) spectroscopy. Based on evidence in the TR-absorption spectra of lattice-decoupled free electron dynamics, they concluded that the resonance was more likely to be due to a plasmon than an IBT.[38] However, they noted that the mode does not show the thickness dependence that would be expected of a transversal LSPR. They posited that this could be due to extreme anisotropy in conductivity, which may restrict electron oscillations to single layers of MXene, eliminating any thickness dependence.

However, there are challenges for such a strongly anisotropic transversal plasmon model. First, out-of-plane modes tend to vanish in the single-layer limit.[72] Second, single-layer plasmons have been investigated in the context of metal−dielectric layered metamaterials (see the inset of Figure 7A) and showed strong interlayer coupling despite interlayer spacings much larger than those of MXenes.[73,74] With a MXene interlayer spacing of 1−2 nm, having uncoupled single layers would imply extraordinary plasmonic confinement on the order of $\sim\lambda/400$.[75] Finally, in multilayer metamaterials, the presence of interlayer plasmonic coupling forms a volume or bulk plasmon, so this hypothesized transversal mode would effectively correspond to a bulk plasmon for the out-of-plane anisotropic dielectric function $\varepsilon'_{zz}(\omega) = 0$ (see section 5).[73,74] The anisotropic dielectric functions in the literature do not show such an out-of-plane zero (Figure 7A).[60]

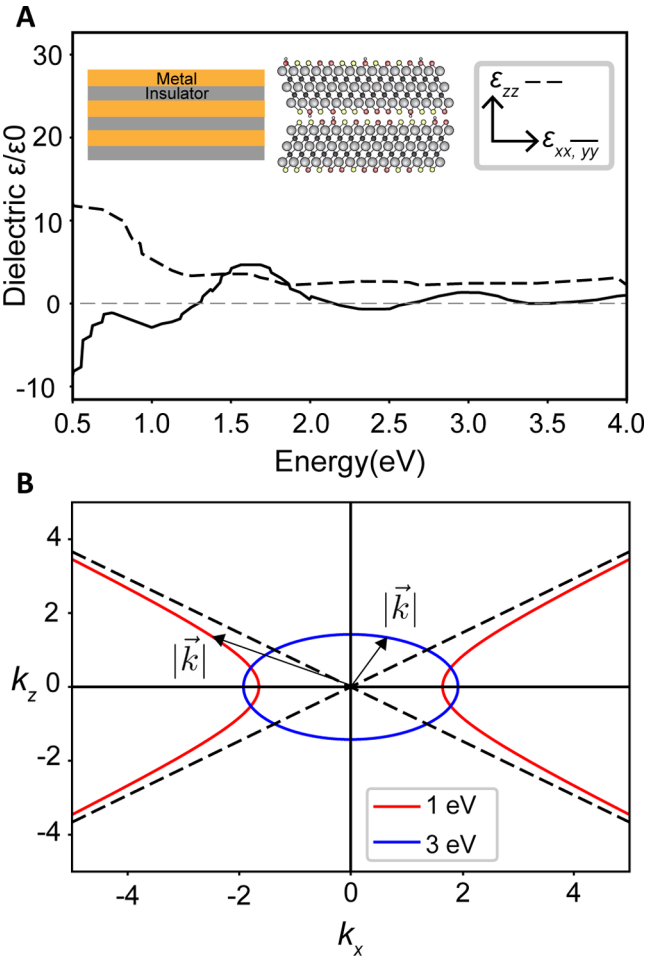

Figure 7. (A) MXenes show structure analogous to multilayer metamaterials, resulting in anisotropic dielectric functions (Lashgari et al. dielectric function is shown here).[60] (B) Isofrequency surfaces $\frac{\omega^2}{c^2} = \frac{k_z^2}{\varepsilon_{xx,yy}(\omega)} + \frac{k_x^2}{\varepsilon_{zz}(\omega)}$ from selected energies (1 and 3 eV) in the dielectric function. The birefringent surface at 3 eV shows elliptical isofrequency surfaces where $\mathrm{sgn}(\varepsilon'_{xx,yy}) = \mathrm{sgn}(\varepsilon'_{zz})$, placing an upper limit on $|\vec{k}|$. Hyperbolic surfaces occur at energies where $\mathrm{sgn}(\varepsilon'_{xx,yy}) \neq \mathrm{sgn}(\varepsilon'_{zz})$ and allow unbounded $|\vec{k}|$.

https://doi.org/10.1021/acs.jpclett.4c02882
J. Phys. Chem. Lett. 2024, 15, 11643−11656

If the 1.7 eV mode is plasmonic, the candidates other than LSPR are a surface plasmon or a bulk plasmon. A surface plasmon should be expected to show spatial variation in the EELS image map due to interferometric effects from edge reflections, which is not observed in the EELS experiments.[29] El-Demellawi et al. also observed this mode for monolayer samples, which would be below the cutoff thickness for s_b SPs but too high in energy for a_b SPs.[27] A bulk plasmon assignment would require $\varepsilon'(\omega) = 0$, a condition met for the dielectric function reported by Shamsabadi et al.[40] A potential issue with the bulk plasmon assignment is the presence of the resonance for monolayer samples, given that bulk plasmons disappear in the single-layer limit.[27,44]

Previous work by our group using PEEM to directly image the plasmonic resonances and dynamics of MXenes showed no evidence of a transverse plasmon resonance. Instead, fringes associated with a surface plasmon polariton were observed when the sample was excited with light in the energy range of interest.[30] This is evidence for the presence of an interband transition near 1.7 eV that causes back-bending of the surface plasmon polariton to the light line before the material can develop a surface plasmon resonance.

Overall, this issue has not yet settled. The literature often does not distinguish between optical and loss function peaks, which along with the large variability in samples may lead to inconsistencies in the type of resonance reported. If there is a region where $\varepsilon'(\omega) < 0$ between ~1.5 and 1.9 eV due to a strong IBT, then there may be both IBT and plasmonic features present in this region. This might account for conflicting observations regarding the nature of the optoelectronic response of MXenes. We argue that the consistent energy and spatial extent of the 1.7 eV mode, which are invariant even considering changes in the thickness and size of MXene flakes and the type of substrate, are more consistent with an interband transition-associated resonance. However, given the complex dependence of $Ti_3C_2T_x$ MXene properties on hard-to-control terminations, assigning the mode in question to a specific electronic transition is difficult. Indeed, new calculations of MXenes coupled with ellipsometry experiments hypothesize that this optical transition is not plasmonic but is caused by oxygen terminations on MXenes.[76] Spectroscopic experiments on single-termination MXenes could help to elucidate the nature of such resonances.

5. ANISOTROPY IN MXenes

MXenes are layered 2D materials with different bonding and interactions in-plane versus out-of-plane. Therefore, they should be best described with an anisotropic dielectric function where the in-plane optoelectronic response along each sheet differs from the out-of-plane response. In MXenes, there is already clear evidence of an order of magnitude difference between in- and out-of-plane conductivity.[49] However, anisotropy has not yet been studied in the context of MXene plasmonics, though it is has been explored for photonic modes in other layered materials such as graphite, hBN, and TMDCs.[63,77,78] Studies on these other anisotropic 2D materials have revealed intriguing phenomena, such as so-called hyperbolic plasmons that allow arbitrarily large k-vectors due to extreme anisotropy.[79,80] These large k-vectors can lead to extreme spatial confinement and field enhancement. Even in less drastic cases, anisotropy may impact the quality and type of plasmonic modes observable in a material.[63,78] Therefore, it is important to consider the role anisotropy could play in MXene plasmonics.

The most general case for anisotropy in 2D materials is that of a uniaxial crystal with a single optical axis in the z (crystallographic c) direction, where the dielectric function tensor has the form $\varepsilon_{xx} = \varepsilon_{yy} \neq \varepsilon_{zz}$. Unfortunately, for most 2D materials, measuring ε_{zz} is much more challenging than measuring $\varepsilon_{xx,yy}$ due to the thinness of the sample that makes normal incidence reflectometry on the flake edge difficult while the small lateral dimensions inhibit oblique angle ellipsometry on the layer plane.[81,82] Due to many of these challenges, experimental work on MXene anisotropy remains lacking, aside from the conductivity measurements by Hu et al.[49] To date, the only anisotropic dielectric functions available for MXenes come from DFT calculations by Lashgari et al.,[60] Xu et al.,[83] and Bai et al.[17] The dielectric function from Lashgari et al. is shown in Figure 7A.

Because of the experimental challenges associated with probing the fully anisotropic dielectric function, the assumption is frequently made that the 2D materials are approximately isotropic, with $\varepsilon \approx \varepsilon_{xx,yy}$.[84] This approximation is most valid for a_b thin-film plasmonic modes in few- or single-layer samples where the electric field is most strongly confined to the in-plane direction, as shown in Figure 5C.

In MXenes, optical measurements of thin-film samples with stacked or overlapping flakes can lead to averaging of the xy and zz properties.[58] Therefore, isotropic dielectric functions from optical measurements often fit the plasmonic dispersion from EELS experiments on single- or few-layer MXenes. However, thicker samples and cases of larger anisotropy may demand a more precise approach than simplification of an isotropic dielectric function.

In particular, other than ellipsometry, experimental anisotropy signatures can appear in the momentum-resolved electron loss spectrum,

$$L(\omega, \boldsymbol{q}) = q^{-2}\,\mathrm{Im}(1/\varepsilon(\omega, \boldsymbol{q})) \tag{11}$$

where $\varepsilon = \varepsilon_{xx,yy}\sin^2\Theta + \varepsilon_{zz}\cos^2\Theta$ and Θ is the angle between the momentum transfer vector $\boldsymbol{q}$ and the c-axis. While difficult, such experiments are feasible at specialized transmission electron microscopy (TEM) and scanning electron microscopy (SEM) facilities worldwide.[85,86] Such experiments could prove critical for understanding the anisotropy of MXenes and provide substantial opportunities for exploring new applications similar to those seen in analogous multilayer metamaterials.

The anisotropic, layered structure of MXenes with surface groups is analogous to that of plasmonic metamaterials such as metal−dielectric multilayer stacks, as shown in the inset in Figure 7A. The total optical response of these multilayered systems can be approximated by a uniaxial effective medium model where $\varepsilon^{\mathrm{eff}}_{xx,yy}$ and $\varepsilon^{\mathrm{eff}}_{zz}$ are determined by the permittivity and thickness of both the metal and dielectric layers.[73,87,88] Because of this, the effective multilayer dielectric function can be precisely controlled by the layer thickness, which allows for tuning of the effective dielectric function. The effective medium model has been extended to 2D materials such as graphite by treating the material as a superlattice of sheets with 2D dielectric $\varepsilon^{\mathrm{2D}}_{xx,yy/zz}$ separated by vacuum.[84] The analogy to a multilayer metamaterial is even more pronounced for MXenes than graphite because intercalation and surface groups in MXenes can create a variable interlayer dielectric environment.[24] Additionally, the transition metal carbide/nitride

https://doi.org/10.1021/acs.jpclett.4c02882
J. Phys. Chem. Lett. 2024, 15, 11643−11656

thickness and interlayer distance can be tuned by the stoichiometry and intercalation of the material due to the synthetic customizability of MXenes. It would be expected that the interaction between MXene sheets, as mediated by the interlayer permittivity, should play a large role in the bulk properties. For example, in metamaterials, tunable coupling between metallic surface plasmons produces a tunable bulk or volume plasmon.[73]

One of the strongest appeals for studying anisotropy in MXenes is the possibility of hyperbolic plasmon regions. Hyperbolic polaritons have already been demonstrated in 2D materials such as α-MoO_3, β-Ga_2O_3, and hBN.[79,89−91] The interest in hyperbolicity stems from the ability to obtain subdiffraction-limit propagating waves in hyperbolic materials. The origin of this phenomenon lies in the wave equation for an anisotropic medium. For uniaxial materials, the wave equation gives the dispersion formula

$$\frac{\omega^2}{c^2} = \frac{k_z^2}{\varepsilon_{xx,yy}(\omega)} + \frac{k_x^2}{\varepsilon_{zz}(\omega)} \tag{12}$$

for p-polarized waves.[73,87] If this equation is plotted in k-space for a single isofrequency slice, the resulting surface is elliptical if $\varepsilon'_{xx,yy}$ and ε'_{zz} have the same sign, as shown in Figure 7B in blue. The closed surface of the ellipse enforces the fundamental diffraction limit, since k-vectors outside the elliptical surface become evanescent. However, in the special case where extreme anisotropy leads to $\mathrm{sgn}(\varepsilon'_{xy}) \neq \mathrm{sgn}(\varepsilon'_{zz})$, the isofrequency surface becomes hyperbolic, shown in Figure 7B in red. The hyperbolic surface is unbounded in k-space, meaning propagating waves of arbitrarily large k-vectors can be hypothetically achieved, thus breaking the optical diffraction limit. Hyperbolic materials can also convert evanescent waves to propagating waves and be used for subdiffraction limit imaging.[80] The increase in $|k|$ also results in a divergence of the photonic density of states (PDOS), which drastically increases the rate of spontaneous emission processes (the Purcell effect).[3,79]

In MXenes, evidence for possible hyperbolic regions comes from the dielectric function reported by Lashgari et al.,[60] shown in Figure 7A, which shows a hyperbolic region below 1.5 eV where $\varepsilon'_{xy} < 0$ due to free electron motion while $\varepsilon'_{zz} > 0$. However, more experimental work is needed to verify this. The intriguing possibility of tuning MXene anisotropy via surface chemistry and intercalation along with relevant hyperbolic applications such as sensing and SERS should prompt increased work in understanding the anisotropic dielectric function of this material.

6. OUTLOOK AND FUTURE DIRECTIONS

Thus far, some of the challenges and promises of MXene plasmonics have been outlined, including some of the disagreements within the literature on bulk plasmon energies and interband transitions for $Ti_3C_2T_x$ and the possibility of hyperbolic plasmons for MXenes. Addressing all of these issues will center around obtaining high-quality MXene dielectric functions or precise electronic band structures. This will help accurately identify both potentially plasmonic regions ($\varepsilon' < 0$), any plasmonic resonances, and regions of large damping (or loss). There are several experimental techniques that could help obtain accurate dielectric functions. Momentum-resolved EELS has the capability to obtain the anisotropic loss function by varying the angle between the momentum transfer $\boldsymbol{q}$ and the crystallographic c axis. This work has been done on other layered materials such as graphite by Marinopoulos et al.[57] An emerging technique for measuring anisotropic dielectric functions is nano-FTIR. This method is performed using scanning near-field optical microscopy (SNOM), which uses a tapping-mode atomic force microscopy (AFM) tip to couple light to the sample below the diffraction limit.[81,92] An advantage to this method is the nanoscale precision, which can account for local variations in electronic structure. However, caution must be taken to accurately model the tip−sample interactions for this method.[93]

Several of the issues discussed in this report suffer from the variable terminations in the mixed-terminated MXene $Ti_3C_2T_x$, which are often difficult to control and characterize. While the HF etching of this material is simple, characterizing the surface terminations is very difficult. For instance, common analysis techniques such as X-ray photoelectron spectroscopy (XPS), nuclear magnetic resonance (NMR), and neutron scattering give drastically different values for surface terminations ratios.[53] MXenes can also suffer from oxidative effects such as intercalation of oxygen into the lattice as oxycarbides.[54] With this in mind, a more precise understanding of the MXene optoelectronic properties will benefit from the use of both single-terminated materials and individual MXene flakes. Fortunately, new developments in synthesis, such as recent efforts by Wang et al.[25] in creating halide-terminated MXenes such as $TiCCl_2$ and Ti_2CBr_2, provide a better route to control material properties.[24,25] This is also an as-of-yet unexplored space for MXene plasmonics, and there has been little exploration of their optoelectronic properties.

As discussed in the previous section, MXenes hold promise as hyperbolic plasmonic materials. The potential for hyperbolicity in MXenes is particularly intriguing, given the structural diversity of these materials. In addition to variability in surface terminations and transition metals, intercalation of small molecules or ions within MXene layers can modulate the interlayer spacing and charge carrier density.[24,53,75,94] The development of MXenes functionalized with organic groups by Zhou et al.[95] provides an excellent opportunity to control this type of interlayer spacing.[24] Thus, the out-of-plane dielectric function as controlled by interlayer spacing and permittivity could be tuned as desired, allowing for the engineering of hyperbolic modes. Additionally, controlling anisotropy not only could enable hyperbolicity but can also improve the quality of guided modes at higher energies where surface plasmons are not allowed, such as those observed by Rieger et al.[30,78] It is important that anisotropic dielectric functions are obtained for a variety of MXenes to determine the role that different structural motifs play in the optical response and what MXene species might be best suited for hyperbolic plasmonics.

MXenes remain a broad material space, and given their diversity and complexity, there remains room for growth within the field. For plasmonics especially, there is great opportunity for exploring new classes of MXenes beyond the mixed-termination case. However, given the wave of attention these materials have received, it is also imperative that great care is taken in both standardizing synthesis and characterization procedures and ensuring that the guidelines of established plasma physics are followed rigorously. With these principles in mind, MXenes should be promising for further innovation and development within the realm of plasmonics.

https://doi.org/10.1021/acs.jpclett.4c02882
J. Phys. Chem. Lett. 2024, 15, 11643−11656

7. METHODS

Simulated electric fields were obtained from analytical Python models. Solutions to Maxwell's equations are found by either analytically solving the semi-infinite dispersion (eq 5) for the two-layer case or numerically solving for poles of the reflection coefficient $r_p(E, k_x)$ in eq 6 for the three-layer model. We select bound modes that evanescently decay away from the interface by choosing $\mathrm{Im}(k_{iz}) > 0$. The electric fields are obtained via the transfer matrix method and plotted in a Jupyter notebook.[96,97] Silicon dioxide dielectric function data was obtained from the SOPRA data bank (https://www.sspectra.com/sopra.html).

■ ASSOCIATED CONTENT

Data Availability Statement

The Python code developed for solving Maxwell's equations for MXenes in various geometries, as shown in Figures 5 and 6, is available on Github at https://github.com/sbking-pchem/verbose-happiness.

■ AUTHOR INFORMATION

Corresponding Author

Sarah B. King − *James Franck Institute, University of Chicago, Chicago, Illinois 60637, United States; Department of Chemistry, University of Chicago, Chicago, Illinois 60637, United States;* orcid.org/0000-0003-0274-9894; Email: sbking@uchicago.edu; http://kinglab.uchicago.edu

Authors

Calvin Raab − *James Franck Institute, University of Chicago, Chicago, Illinois 60637, United States; Department of Chemistry, University of Chicago, Chicago, Illinois 60637, United States;* orcid.org/0009-0005-5633-3992

Janek Rieger − *James Franck Institute, University of Chicago, Chicago, Illinois 60637, United States*

Atreyie Ghosh − *James Franck Institute, University of Chicago, Chicago, Illinois 60637, United States*

Joseph L. Spellberg − *James Franck Institute, University of Chicago, Chicago, Illinois 60637, United States; Department of Chemistry, University of Chicago, Chicago, Illinois 60637, United States*

Complete contact information is available at: https://pubs.acs.org/10.1021/acs.jpclett.4c02882

Notes

The authors declare no competing financial interest.

Biographies

Calvin Raab is a Ph.D. student in the Chemistry Department of the University of Chicago. He received his Bachelor of Science in Chemistry from Grove City College in Pennsylvania in 2022. His research focuses on imaging and modeling the nanoscale plasmonic properties of low-dimensional materials.

Janek Rieger is a former postdoctoral researcher in the James Franck Institute of the University of Chicago. He obtained his Bachelors (2015) and Masters (2017) of Science in Physics and Ph.D. (2022) in Physics at Friedrich-Alexander-Universität Erlangen-Nürnberg in Germany. His research focuses on applying photoemission electron microscopy to complex material systems.

Atreyie Ghosh is a Kadanoff-Rice Postdoctoral fellow in the James Franck Institute of the University of Chicago. She obtained her Bachelor of Science in Physics at St. Xaviers College, Kolkata, India in 2014, her Master of Science in Physics at the Indian Institute of Technology Madras in 2016, and her Ph.D. in Physics at the University of Pittsburgh in 2023. Her research focuses on imaging plasmonic and nanoscale domains in low-dimensional materials.

Joseph L. Spellberg is a Ph.D. student in the Chemistry Department of the University of Chicago. He received his Bachelor of Arts in Chemistry at Washington University in St. Louis in 2020. His research focuses on imaging nanoscale domains in low-dimensional materials.

Sarah B. King is an Assistant Professor of Chemistry at the University of Chicago. She received her Bachelor of Science in Chemistry at the Massachusetts Institute of Technology in 2010 and her Ph.D. in Chemistry in 2015 at the University of California, Berkeley. She was an Alexander von Humboldt postdoctoral fellow at the Fritz Haber Institute of the Max Planck Society in Berlin, Germany from 2015-2018. Her research group aims to probe nanoscale structure and dynamics of materials and interfaces.

■ ACKNOWLEDGMENTS

This work was funded by the U.S. Air Force Office of Scientific Research (FA9550-22-1-0224). A.G. acknowledges support from a UChicago Materials Research Science and Engineering Center Kadanoff-Rice fellowship funded by the NSF under award number DMR-2011854.

■ REFERENCES

(1) Novoselov, K. S.; Mishchenko, A.; Carvalho, A.; Neto, A. H. C. 2D materials and van der Waals heterostructures. *Science* **2016**, *353*, aac9439.

(2) Yu, S.; Wu, X.; Wang, Y.; Guo, X.; Tong, L. 2d materials for optical modulation: Challenges and opportunities. *Adv. Mater.* **2017**, *29*, 1606128.

(3) Elbanna, A.; Jiang, H.; Fu, Q.; Zhu, J.-F.; Liu, Y.; Zhao, M.; Liu, D.; Lai, S.; Chua, X. W.; Pan, J.; Shen, Z. X.; Wu, L.; Liu, Z.; Qiu, C.-W.; Teng, J. 2D material infrared photonics and plasmonics. *ACS Nano* **2023**, *17*, 4134−4179.

(4) Basov, D. N.; Fogler, M. M.; Abajo, F. J. G. d. Polaritons in van der Waals materials. *Science* **2016**, *354*, eaag1992.

(5) Li, Y.; Li, Z.; Chi, C.; Shan, H.; Zheng, L.; Fang, Z. Plasmonics of 2D nanomaterials: Properties and applications. *Adv. Sci.* **2017**, *4*, 1600430.

(6) Grigorenko, A. N.; Polini, M.; Novoselov, K. S. Graphene plasmonics. *Nat. Photonics* **2012**, *6*, 749−758.

(7) Basov, D. N.; Asenjo-Garcia, A.; Schuck, P. J.; Zhu, X.; Rubio, A. Polariton panorama. *Nanophotonics* **2020**, *10*, 549−577.

(8) Barnes, W. L.; Dereux, A.; Ebbesen, T. W. Surface plasmon subwavelength optics. *Nature* **2003**, *424*, 824−830.

(9) Guo, X.; Lyu, W.; Chen, T.; Luo, Y.; Wu, C.; Yang, B.; Sun, Z.; Abajo, F. J. G. d.; Yang, X.; Dai, Q. Polaritons in van der Waals heterostructures. *Adv. Mater.* **2023**, *35*, No. e2201856.

(10) Fei, Z.; Rodin, A. S.; Andreev, G. O.; Bao, W.; McLeod, A. S.; Wagner, M.; Zhang, L. M.; Zhao, Z.; Thiemens, M.; Dominguez, G.; Fogler, M. M.; Neto, A. H. C.; Lau, C. N.; Keilmann, F.; Basov, D. N. Gate-tuning of graphene plasmons revealed by infrared nano-imaging. *Nature* **2012**, *487*, 82−85.

(11) Gonçalves, P. A. D. *Plasmonics and Light−Matter Interactions in Two-Dimensional Materials and in Metal Nanostructures, Classical and Quantum Considerations*; Springer Theses: Cham, 2020.

(12) Zhang, D.; Shah, D.; Boltasseva, A.; Gogotsi, Y. MXenes for photonics. *ACS Photonics* **2022**, *9*, 1108−1116.

(13) Jiang, X.; Kuklin, A. V.; Baev, A.; Ge, Y.; Ågren, H.; Zhang, H.; Prasad, P. N. Two-dimensional MXenes: From morphological to optical, electric, and magnetic properties and applications. *Phys. Rep.* **2020**, *848*, 1−58.

(14) Hu, T.; Hu, M.; Li, Z.; Zhang, H.; Zhang, C.; Wang, J.; Wang, X. Interlayer coupling in two-dimensional titanium carbide MXenes. *Phys. Chem. Chem. Phys.* **2016**, *18*, 20256−20260.

(15) Gogotsi, Y. The future of MXenes. *Chem. Mater.* **2023**, *35*, 8767−8770.
(16) Khazaei, M.; Ranjbar, A.; Arai, M.; Sasaki, T.; Yunoki, S. Electronic properties and applications of MXenes: a theoretical review. *J. Mater. Chem. C* **2017**, *5*, 2488−2503.
(17) Bai, Y.; Zhou, K.; Srikanth, N.; Pang, J. H. L.; He, X.; Wang, R. Dependence of elastic and optical properties on surface terminated groups in two-dimensional MXene monolayers: a first-principles study. *RSC Adv.* **2016**, *6*, 35731−35739.
(18) Gogotsi, Y.; Anasori, B. The rise of MXenes. *ACS Nano* **2019**, *13*, 8491−8494.
(19) Zhang, Y.-Z.; Wang, Y.; Jiang, Q.; El-Demellawi, J. K.; Kim, H.; Alshareef, H. N. MXene printing and patterned coating for device applications. *Adv. Mater.* **2020**, *32*, No. e1908486.
(20) Shahzad, F.; Alhabeb, M.; Hatter, C. B.; Anasori, B.; Hong, S. M.; Koo, C. M.; Gogotsi, Y. Electromagnetic interference shielding with 2D transition metal carbides (MXenes). *Science* **2016**, *353*, 1137−1140.
(21) Yun, T.; Kim, H.; Iqbal, A.; Cho, Y. S.; Lee, G. S.; Kim, M.-K.; Kim, S. J.; Kim, D.; Gogotsi, Y.; Kim, S. O.; Koo, C. M. Electromagnetic shielding of monolayer MXene assemblies. *Adv. Mater.* **2020**, *32*, No. e1906769.
(22) Kamysbayev, V.; Filatov, A. S.; Hu, H.; Rui, X.; Lagunas, F.; Wang, D.; Klie, R. F.; Talapin, D. V. Covalent surface modifications and superconductivity of two-dimensional metal carbide MXenes. *Science* **2020**, *369*, 979−983.
(23) Wu, Q.; Xue, Y.; Chao, S.; Wu, F.; Li, L.; Javed, M. S.; Zhang, W. Moiré superlattice MXene nanosheets constructed from twisted hexagon-Ti_3AlC_2 by microwave-assisted lewis molten salt etching: Implications for structural stability in electrochemical energy storage. *ACS Appl. Nano Mater.* **2023**, *6*, 677−684.
(24) Jiang, M.; Wang, D.; Kim, Y.-H.; Duan, C.; Talapin, D.; Zhou, C. Evolution of surface chemistry in two-dimensional mxenes: from mixed to tunable uniform terminations. *Angew. Chem.* **2024**, *136*, No. e202409480.
(25) Wang, D.; Zhou, C.; Filatov, A. S.; Cho, W.; Lagunas, F.; Wang, M.; Vaikuntanathan, S.; Liu, C.; Klie, R. F.; Talapin, D. V. Direct synthesis and chemical vapor deposition of 2D carbide and nitride MXenes. *Science* **2023**, *379*, 1242−1247.
(26) Mauchamp, V.; Bugnet, M.; Bellido, E. P.; Botton, G. A.; Moreau, P.; Magne, D.; Naguib, M.; Cabioc'h, T.; Barsoum, M. W. Enhanced and tunable surface plasmons in two-dimensional Ti_3C_2 stacks: Electronic structure versus boundary effects. *Phys. Rev. B* **2014**, *89*, 235428.
(27) El-Demellawi, J. K.; Lopatin, S.; Yin, J.; Mohammed, O. F.; Alshareef, H. N. Tunable multipolar surface plasmons in 2D $Ti_3C_2T_x$ MXene flakes. *ACS Nano* **2018**, *12*, 8485−8493.
(28) Bilyk, T.; Hsiao, H.-W.; Yuan, R.; Benchakar, M.; Habrioux, A.; Célérier, S.; Zuo, J.-M.; Pacaud, J.; Mauchamp, V. Plasmon spectroscopy for the determination of $Ti_3C_2T_x$ MXene few layer stacks architecture. *2D Mater.* **2022**, *9*, 035017.
(29) Guo, X.; Li, N.; Wu, C.; Dai, X.; Qi, R.; Qiao, T.; Su, T.; Lei, D.; Liu, N.; Du, J.; Wang, E.; Yang, X.; Gao, P.; Dai, Q. Studying plasmon dispersion of MXene for enhanced electromagnetic absorption. *Adv. Mater.* **2022**, *34*, No. e2201120.
(30) Rieger, J.; Ghosh, A.; Spellberg, J.; Raab, C.; Mohan, A.; Joshi, P.; King, S. Imaging and simulation of surface plasmon polaritons on layered 2D MXenes. *ChemRxiv Preprint* **2024**, DOI: 10.26434/chemrxiv-2024-sl7t4.
(31) Berini, P. Long-range surface plasmon polaritons. *Adv. Opt. Photonics* **2009**, *1*, 484.
(32) Sarycheva, A.; Makaryan, T.; Maleski, K.; Satheeshkumar, E.; Melikyan, A.; Minassian, H.; Yoshimura, M.; Gogotsi, Y. Two-dimensional titanium carbide (MXene) as surface-enhanced raman scattering substrate. *J. Phys. Chem. C* **2017**, *121*, 19983−19988.
(33) Velusamy, D. B.; El-Demellawi, J. K.; El-Zohry, A. M.; Giugni, A.; Lopatin, S.; Hedhili, M. N.; Mansour, A. E.; Fabrizio, E. D.; Mohammed, O. F.; Alshareef, H. N. MXenes for plasmonic photodetection. *Adv. Mater.* **2019**, *31*, No. e1807658.
(34) Fan, X.; Ding, Y.; Liu, Y.; Liang, J.; Chen, Y. Plasmonic $Ti_3C_2T_x$ MXene enables highly efficient photothermal conversion for healable and transparent wearable device. *ACS Nano* **2019**, *13*, 8124−8134.
(35) Morales-Garcia, A.; Calle-Vallejo, F.; Illas, F. MXenes: New horizons in catalysis. *ACS Catal.* **2020**, *10*, 13487−13503.
(36) Li, G.; Kushnir, K.; Dong, Y.; Chertopalov, S.; Rao, A. M.; Mochalin, V. N.; Podila, R.; Titova, L. V. Equilibrium and non-equilibrium free carrier dynamics in 2D $Ti_3C_2T_x$ MXenes: THz spectroscopy study. *2D Mater.* **2018**, *5*, 035043.
(37) Miranda, A.; Halim, J.; Barsoum, M. W.; Lorke, A. Electronic properties of freestanding $Ti_3C_2T_x$ MXene monolayers. *Appl. Phys. Lett.* **2016**, *108*, 033102.
(38) Lioi, D. B.; Stevenson, P. R.; Seymour, B. T.; Neher, G.; Schaller, R. D.; Gosztola, D. J.; Vaia, R. A.; Vernon, J. P.; Kennedy, W. J. Simultaneous ultrafast transmission and reflection of nanometer-thick $Ti_3C_2T_x$ MXene films in the visible and near-infrared: Implications for energy storage, electromagnetic shielding, and laser systems. *ACS Appl. Nano Mater.* **2020**, *3*, 9604−9609.
(39) Chaudhuri, K.; Alhabeb, M.; Wang, Z.; Shalaev, V. M.; Gogotsi, Y.; Boltasseva, A. Highly broadband absorber using plasmonic titanium carbide (MXene). *ACS Photonics* **2018**, *5*, 1115−1122.
(40) Shamsabadi, A. A.; Fang, H.; Zhang, D.; Thakur, A.; Chen, C. Y.; Zhang, A.; Wang, H.; Anasori, B.; Soroush, M.; Gogotsi, Y.; Fakhraai, Z. The evolution of MXenes conductivity and optical properties upon heating in air. *Small Methods* **2023**, *7*, No. e2300568.
(41) Dillon, A. D.; Ghidiu, M. J.; Krick, A. L.; Griggs, J.; May, S. J.; Gogotsi, Y.; Barsoum, M. W.; Fafarman, A. T. Highly conductive optical quality solution-processed films of 2D titanium carbide. *Adv. Funct. Mater.* **2016**, *26*, 4162−4168.
(42) Raether, H. *Excitation of Plasmons and Interband Transitions by Electrons*, Springer Tracts in Modern Physics, Vol. *88*; Springer-Verlag: Berlin Heidelberg, 1980.
(43) Wang, Y.; Plummer, E. W.; Kempa, K. Foundations of plasmonics. *Adv. Phys.* **2011**, *60*, 799−898.
(44) Egerton, R. *Electron Energy Loss Spectroscopy in the Electron Microscope*; Springer, 1996.
(45) Liu, M.; Pelton, M.; Guyot-Sionnest, P. Reduced damping of surface plasmons at low temperatures. *Phys. Rev. B* **2009**, *79*, 035418.
(46) Pitarke, J. M.; Silkin, V. M.; Chulkov, E. V.; Echenique, P. M. Theory of surface plasmons and surface-plasmon polaritons. *Rep. Prog. Phys.* **2007**, *70*, 1.
(47) Smith, D. Y.; Segall, B. Intraband and interband processes in the infrared spectrum of metallic aluminum. *Phys. Rev. B* **1986**, *34*, 5191−5198.
(48) Hartstein, K. H.; Schimpf, A. M.; Salvador, M.; Gamelin, D. R. Cyclotron splittings in the plasmon resonances of electronically doped semiconductor nanocrystals probed by magnetic circular dichroism spectroscopy. *J. Phys. Chem. Lett.* **2017**, *8*, 1831−1836.
(49) Hu, T.; Zhang, H.; Wang, J.; Li, Z.; Hu, M.; Tan, J.; Hou, P.; Li, F.; Wang, X. Anisotropic electronic conduction in stacked two-dimensional titanium carbide. *Sci. Rep.* **2015**, *5*, 16329.
(50) Shekhirev, M.; Busa, J.; Shuck, C. E.; Torres, A.; Bagheri, S.; Sinitskii, A.; Gogotsi, Y. Ultralarge flakes of $Ti_3C_2T_x$ MXene via soft delamination. *ACS Nano* **2022**, *16*, 13695−13703.
(51) Alhabeb, M.; Maleski, K.; Anasori, B.; Lelyukh, P.; Clark, L.; Sin, S.; Gogotsi, Y. Guidelines for synthesis and processing of two-dimensional titanium carbide ($Ti_3C_2T_x$ MXene). *Chem. Mater.* **2017**, *29*, 7633−7644.
(52) Hantanasirisakul, K.; Alhabeb, M.; Lipatov, A.; Maleski, K.; Anasori, B.; Salles, P.; Ieosakulrat, C.; Pakawatpanurut, P.; Sinitskii, A.; May, S. J.; Gogotsi, Y. Effects of synthesis and processing on optoelectronic properties of titanium carbonitride MXene. *Chem. Mater.* **2019**, *31*, 2941−2951.
(53) Natu, V.; Barsoum, M. W. MXene surface terminations: A perspective. *J. Phys. Chem. C* **2023**, *127*, 20197−20206.
(54) Michałowski, P.ł P.; Anayee, M.; Mathis, T. S.; Kozdra, S.; Wojcik, A.; Hantanasirisakul, K.; Jozwik, I.; Piatkowska, A.; Mozdzonek, M.łg.; Malinowska, A.; Diduszko, R.; Wierzbicka, E.; Gogotsi, Y. Oxycarbide MXenes and MAX phases identification using

monoatomic layer-by-layer analysis with ultralow-energy secondary-ion mass spectrometry. *Nat. Nanotechnol.* **2022**, *17*, 1192−1197.
(55) Zheng, W.; Sun, B.; Li, D.; Gali, S. M.; Zhang, H.; Fu, S.; Di Virgilio, L.; Li, Z.; Yang, S.; Zhou, S.; Beljonne, D.; Yu, M.; Feng, X.; Wang, H. I.; Bonn, M. Band transport by large fröhlich polarons in MXenes. *Nat. Phys.* **2022**, *18*, 544−550.
(56) Raether, H. *Surface Plasmons on Smooth and Rough Surfaces and on Gratings*, Springer Tracts in Modern Physics; Springer: Berlin, Heidelberg, 1988.
(57) Marinopoulos, A. G.; Reining, L.; Olevano, V.; Rubio, A.; Pichler, T.; Liu, X.; Knupfer, M.; Fink, J. Anisotropy and interplane interactions in the dielectric response of graphite. *Phys. Rev. Lett.* **2002**, *89*, 076402.
(58) Mauchamp, V.; Yu, W.; Gence, L.; Piraux, L.; Cabioc'h, T.; Gauthier, V.; Eklund, P.; Dubois, S. Anisotropy of the resistivity and charge-carrier sign in nanolaminated Ti_2AlC: Experiment and ab initio calculations. *Phys. Rev. B* **2013**, *87*, 235105.
(59) Olafsson, A.; Busche, J. A.; Araujo, J. J.; Maiti, A.; Idrobo, J. C.; Gamelin, D. R.; Masiello, D. J.; Camden, J. P. Electron beam infrared nano-ellipsometry of individual indium tin oxide nanocrystals. *Nano Lett.* **2020**, *20*, 7987−7994.
(60) Lashgari, H.; Abolhassani, M.; Boochani, A.; Elahi, S.; Khodadadi, J. Electronic and optical properties of 2D graphene-like compounds titanium carbides and nitrides: Dft calculations. *Solid State Commun.* **2014**, *195*, 61−69.
(61) Berdiyorov, G. R. Optical properties of functionalized $Ti_3C_2T_2$ (T = F, O, OH) MXene: First-principles calculations. *AIP Adv.* **2016**, *6*, 055105.
(62) Panova, D. A.; Tselikov, G. I.; Ermolaev, G. A.; Syuy, A. V.; Zimbovskii, D. S.; Kapitanova, O. O.; Yakubovsky, D. I.; Mazitov, A. B.; Kruglov, I. A.; Vyshnevyy, A. A.; Arsenin, A. V.; Volkov, V. S. Broadband optical properties of Ti_3C_2 MXene revisited. *Opt. Lett.* **2024**, *49*, 25.
(63) Warmbier, R.; Manyali, G. S.; Quandt, A. Surface plasmon polaritons in lossy uniaxial anisotropic materials. *Phys. Rev. B* **2012**, *85*, 085442.
(64) Campione, S.; Brener, I.; Marquier, F. Theory of epsilon-near-zero modes in ultrathin films. *Phys. Rev. B* **2015**, *91*, 121408.
(65) Archambault, A.; Teperik, T. V.; Marquier, F.; Greffet, J. J. Surface plasmon fourier optics. *Phys. Rev.B* **2009**, *79*, 195414.
(66) Cherqui, C.; Thakkar, N.; Li, G.; Camden, J. P.; Masiello, D. J. Characterizing localized surface plasmons using electron energy-loss spectroscopy. *Annu. Rev. Phys. Chem.* **2016**, *67*, 331−357.
(67) Bigelow, N. W.; Vaschillo, A.; Iberi, V.; Camden, J. P.; Masiello, D. J. Characterization of the electron- and photon-driven plasmonic excitations of metal nanorods. *ACS Nano* **2012**, *6*, 7497−7504.
(68) Cui, L.; Wang, J.; Sun, M. Graphene plasmon for optoelectronics. *Rev. Mod. Phys.* **2021**, *6*, 100054.
(69) Yuan, H. Y.; Blanter, Y. M. Breaking surface-plasmon excitation constraint via surface spin waves. *Phys. Rev. Lett.* **2024**, *133*, 156703.
(70) Glor, E. C.; Ferrier, R. C.; Li, C.; Composto, R. J.; Fakhraai, Z. Out-of-plane orientation alignment and reorientation dynamics of gold nanorods in polymer nanocomposite films. *Soft Matter* **2017**, *13*, 2207−2215.
(71) Maleski, K.; Shuck, C. E.; Fafarman, A. T.; Gogotsi, Y. The broad chromatic range of two-dimensional transition metal carbides. *Adv. Opt. Mater.* **2021**, *9*, 2001563.
(72) Eberlein, T.; Bangert, U.; Nair, R. R.; Jones, R.; Gass, M.; Bleloch, A. L.; Novoselov, K. S.; Geim, A.; Briddon, P. R. Plasmon spectroscopy of free-standing graphene films. *Phys. Rev. B* **2008**, *77*, 233406.
(73) Zhukovsky, S. V.; Kidwai, O.; Sipe, J. E. Physical nature of volume plasmon polaritons in hyperbolic metamaterials. *Opt. Express* **2013**, *21*, 14982.
(74) Zhukovsky, S. V.; Andryieuski, A.; Sipe, J. E.; Lavrinenko, A. V. From surface to volume plasmons in hyperbolic metamaterials: General existence conditions for bulk high-k waves in metal-dielectric and graphene-dielectric multilayers. *Phys. Rev. B* **2014**, *90*, 155429.
(75) Simon, P. Two-dimensional MXene with controlled interlayer spacing for electrochemical energy storage. *ACS Nano* **2017**, *11*, 2393−2396.
(76) Fang, H.; Fang, Z.; Thakur, A.; Anasori, B.; Rappe, A. M.; Fakhraai, Z. Signatures of band-like optical and charge transport in $Ti_3C_2T_x$ mxene flakes. *ChemRxiv Preprint* **2024**, DOI: 10.26434/chemrxiv-2024-rpf17.
(77) Dai, S.; Fei, Z.; Ma, Q.; Rodin, A. S.; Wagner, M.; McLeod, A. S.; Liu, M. K.; Gannett, W.; Regan, W.; Watanabe, K.; Taniguchi, T.; Thiemens, M.; Dominguez, G.; Neto, A. H. C.; Zettl, A.; Keilmann, F.; Jarillo-Herrero, P.; Fogler, M. M.; Basov, D. N. Tunable phonon polaritons in atomically thin van der Waals crystals of boron nitride. *Science* **2014**, *343*, 1125−1129.
(78) Ermolaev, G. A.; Grudinin, D. V.; Stebunov, Y. V.; Voronin, K. V.; Kravets, V. G.; Duan, J.; Mazitov, A. B.; Tselikov, G. I.; Bylinkin, A.; Yakubovsky, D. I.; Novikov, S. M.; Baranov, D. G.; Nikitin, A. Y.; Kruglov, I. A.; Shegai, T.; Alonso-González, P.; Grigorenko, A. N.; Arsenin, A. V.; Novoselov, K. S.; Volkov, V. S. Giant optical anisotropy in transition metal dichalcogenides for next-generation photonics. *Nat. Commun.* **2021**, *12*, 854.
(79) Gjerding, M. N.; Petersen, R.; Pedersen, T. G.; Mortensen, N. A.; Thygesen, K. S. Layered van der Waals crystals with hyperbolic light dispersion. *Nat. Commun.* **2017**, *8*, 320.
(80) Sun, J.; Litchinitser, N. M.; Zhou, J. Indefinite by nature: From ultraviolet to terahertz. *ACS Photonics* **2014**, *1*, 293−303.
(81) Ruta, F. L.; Sternbach, A. J.; Dieng, A. B.; McLeod, A. S.; Basov, D. N. Quantitative nanoinfrared spectroscopy of anisotropic van der Waals materials. *Nano Lett.* **2020**, *20*, 7933−7940.
(82) Liang, W. Y. Optical anisotropy in layer compounds. *J. Phys. C: Solid State Phys.* **1973**, *6*, 551.
(83) Xu, M.; Yang, J.; Liu, L. Temperature-dependent optical and electrical properties of bulk Ti_2AlC and two-dimensional MXenes from first-principles. *Physica B Condens. Matter* **2019**, *560*, 146−154.
(84) Matthes, L.; Pulci, O.; Bechstedt, F. Influence of out-of-plane response on optical properties of two-dimensional materials: First principles approach. *Phys. Rev. B* **2016**, *94*, 205408.
(85) Zeiger, P.; Hachtel, J.; Legut, D.; Janzen, E.; Barthel, J.; Edgar, J. H.; Allen, L. J.; Rusz, J. Control of the phonon band gap with isotopes in hexagonal boron nitride. *arXiv Preprint* **2023**, DOI: 10.48550/arxiv.2302.13415.
(86) Rossi, A. W.; Bourgeois, M. R.; Walton, C.; Masiello, D. J. Probing the polarization of low-energy excitations in 2D materials from atomic crystals to nanophotonic arrays using momentum-resolved electron energy loss spectroscopy. *Nano Lett.* **2024**, *24*, 7748−7756.
(87) Schilling, J. Uniaxial metallo-dielectric metamaterials with scalar positive permeability. *Phys. Rev. E* **2006**, *74*, 046618.
(88) Papadakis, G. T.; Yeh, P.; Atwater, H. A. Retrieval of material parameters for uniaxial metamaterials. *Phys. Rev. B* **2015**, *91*, 155406.
(89) Matson, J.; Wasserroth, S.; Ni, X.; Obst, M.; Diaz-Granados, K.; Carini, G.; Renzi, E. M.; Galiffi, E.; Folland, T. G.; Eng, L. M.; Klopf, J. M.; Mastel, S.; Armster, S.; Gambin, V.; Wolf, M.; Kehr, S. C.; Alù, A.; Paarmann, A.; Caldwell, J. D. Controlling the propagation asymmetry of hyperbolic shear polaritons in beta-gallium oxide. *Nat. Commun.* **2023**, *14*, 5240.
(90) Dai, S.; Ma, Q.; Andersen, T.; Mcleod, A. S.; Fei, Z.; Liu, M. K.; Wagner, M.; Watanabe, K.; Taniguchi, T.; Thiemens, M.; Keilmann, F.; Jarillo-Herrero, P.; Fogler, M. M.; Basov, D. N. Subdiffractional focusing and guiding of polaritonic rays in a natural hyperbolic material. *Nat. Commun.* **2015**, *6*, 6963.
(91) Enders, M. T.; Sarkar, M.; Giteau, M.; Deeva, A.; Sheinfux, H. H.; Shokooh-Saremi, M.; Koppens, F. H. L.; Papadakis, G. T. Deeply subwavelength mid-infrared phase retardation with α-MoO_3 flakes. *Commun. Mater.* **2024**, *5*, 16.
(92) Keilmann, F.; Hillenbrand, R. Near-field microscopy by elastic light scattering from a tip. *Philos. Trans. Royal Soc. A* **2004**, *362*, 787−805.
(93) García-Etxarri, A.; Romero, I.; Abajo, F. J. G. d.; Hillenbrand, R.; Aizpurua, J. Influence of the tip in near-field imaging of

nanoparticle plasmonic modes: Weak and strong coupling regimes. *Phys. Rev. B* **2009**, *79*, 125439.
(94) Hart, J. L.; Hantanasirisakul, K.; Lang, A. C.; Anasori, B.; Pinto, D.; Pivak, Y.; Omme, J. T. v.; May, S. J.; Gogotsi, Y.; Taheri, M. L. Control of MXenes' electronic properties through termination and intercalation. *Nat. Commun.* **2019**, *10*, 522.
(95) Zhou, C.; Wang, D.; Lagunas, F.; Atterberry, B.; Lei, M.; Hu, H.; Zhou, Z.; Filatov, A. S.; Jiang, D.-e.; Rossini, A. J.; Klie, R. F.; Talapin, D. V. Hybrid organic−inorganic two-dimensional metal carbide MXenes with amido- and imido-terminated surfaces. *Nat. Chem.* **2023**, *15*, 1722−1729.
(96) Wendler, L.; Haupt, R. Long-range surface plasmon-phonon-polaritons. *J. Phys. C: Solid State Phys.* **1986**, *19*, 1871.
(97) Passler, N. C.; Paarmann, A. Generalized 4 × 4 matrix formalism for light propagation in anisotropic stratified media: study of surface phonon polaritons in polar dielectric heterostructures. *J. Opt. Soc. Am. B* **2017**, *34*, 2128−2139.

https://doi.org/10.1021/acs.jpclett.4c02882
J. Phys. Chem. Lett. 2024, 15, 11643−11656